An Experimental Platform for Optimization of Dynamic Causal Modeling-Based Analysis of Functional Neuroimaging Data

R.L. Barbour[1,2], H.L Graber[1,2], C.H. Schmitz[3,4], D.S. Pfeil[2], D.C Lee[2], Y. Xu[1,2]

[1]*NIRx Medical Technologies, Glen Head, NY,* [2]*SUNY Downstate Medical Center, Brooklyn, NY,*
[3]*NIRx Medizintechnik GmbH, Berlin,* [4]*Charite Univeritatsmedizin, Berlin*

Introduction

- Brain-computer interface (BCI) applications often use either invasive electrodes or non-invasive measures that have mobility limitations (e.g., fMRI). An alternative is ***functional near infrared spectroscopic (fNIRS) imaging***, which has the spatial resolution needed to localize activation in the somatosensory cortex [1], and it is more mobile than other non-invasive methods [2].
- In addition to direct measures of activation, and to studies of *structural* connectivity (explored by, e.g., diffusion tensor MRI [3]), steadily increasing use is being made of methods for estimating *functional* or *effective* connectivity.
  - A PubMed search of papers published in the last five years yielded 2037(337) on the subject of functional(effective) connectivity, 81%(84%) of them fMRI-based.
- Effective connectivity algorithms (e.g., dynamic causal modeling, or DCM [4]) frequently make assumptions regarding system behavior (e.g., neurovascular coupling model) that are not easily validated. Also, in practice there isn't a way to confirm that the conclusion drawn from a connectivity analysis is correct.
  - Simulation studies have been conducted, which show that under the modeled conditions DCM will select the correct effective connectivity network from a set of plausible hypotheses. [5]
  - Extension of the preceding to an experimental environment would require a corresponding level of a priori knowledge of the "ground truth."
- Here we present a testbed for fNIRS imaging, which includes a stable solid-state phantom containing embedded electrochromic and electric-dipole elements. The behavior of the internal devices are user-controlled and programmable, such that they can be used to mimic position-dependent and time-varying hemodynamic and bioelectric responses.
  - Additional aspects of the testbed include a support environment for the phantom, including integrated sensing headgear and a robust data analysis environment that can infer effective connectivity based on DCM.
  - As a demonstration of the utility of the testbed, we have carried out a set of experiments and data analyses—based on and extending a simulation study reported in Ref. 5—to assess the robustness of results obtained from DCM-based model-selection computations.

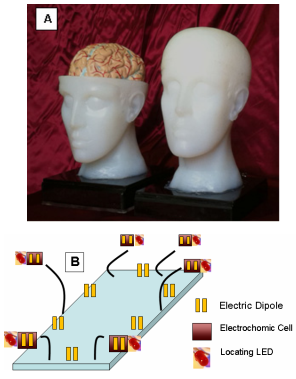

Fig. 1. A: Partially and fully formed anthropomorphic head phantoms. B: Schematic of embedded source array containing electric dipoles, ECCs and locating LEDs.

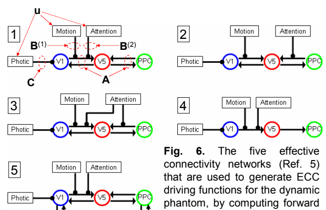

Fig. 6. The five effective connectivity networks (Ref. 5) that are used to generate ECC driving functions for the dynamic phantom, by computing forward solutions to Eqs. (1) and (2). The same five are subsequently used as connectivity hypotheses for the DCM inverse-problem solver. The correspondence between connections and the matrices in Eq. (1) are labeled.

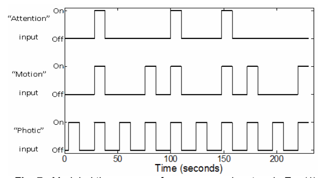

Fig. 7. Modeled time courses for exogenous inputs **u** in Eq. (1)

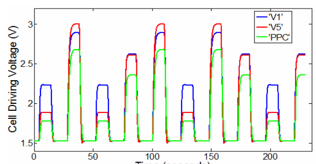

Fig. 8. Time courses of the driving voltages delivered to the ECCs that model the hemodynamic responses of the indicated cortical regions. Indicated voltages are proportional to tissue blood volume values computed by evaluating the DCM forward problem.

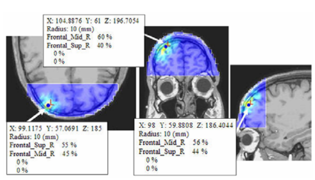

Fig. 9. Recovered spatial information (colored regions) for a selected ECC in the programmable phantom, overlaid onto the structural MRI used in the computation of image reconstruction operator. Plotted quantity is the value of the GLM β coefficient obtained by fitting the driving function to the tissue blood volume time series in each image pixel. β values are well-localized in all dimensions, and the AAL information shows they are assigned to the same anatomical structures in all dimensions.

Acknowledgements

This work was supported by the Defense Advanced Research Projects Agency ; by the NIH under grant nos. R21NS067278, R42NS050007 and 5R44NS049734;by the New York State Department of Health; and by EU grants NEST 012778, EFRE 200020062/6, and nEUROpt 201076.

Methods

- Solid-State Dynamic Phantom (**Fig. 1**)
  - Anthropomorphic (or other biological forms (see Fig. 6A)), air-tight, and resistant to biological degradation
  - Matrix consists of silicone and saline-based biopolymer
  - Electrochromic cells (ECC) mimic wavelength-dependent hemodynamic responses
  - Electric dipoles mimic bioelectric responses
  - Connectors for user interface and controlling electronics are built into the base of the phantom (see Fig. 2B).
- Sensing and Headgear
  - NIRx NIRScout imaging system
    - Accommodates up to 32 detectors and 48 sources, time-multiplexed with adjustable gain switching [2,6]
    - 16 detectors and 16 dual-wavelength superluminescent LEDs operating at 760 and 850 nm were used
  - NIRx DYNOT Compact imaging system
    - Accommodates up to 32 detectors and 9 sources, time-multiplexed with adjustable gain switching
    - 30 detectors and 9 dual-wavelength diode-laser sources operating at 760 and 830 nm were used
  - Headgear in either case was a modified Easy-Cap from Brain Products (**Fig. 2**) [7]

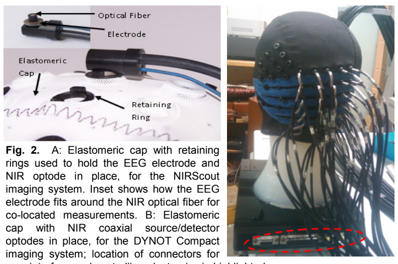

Fig. 2. A: Elastomeric cap with retaining rings used to hold the EEG electrode and NIR optode in place, for the NIRScout imaging system. Inset shows how the EEG electrode fits around the NIR optical fiber for co-located measurements. B: Elastomeric cap with NIR coaxial source/detector optodes in place, for the DYNOT Compact imaging system; location of connectors for user interface and controlling electronics is highlighted.

- NAVI-SPM and Mapping Environment
  - NAVI (Near-Infrared, Analysis, Visualization and Imaging) (**Fig. 3**) [8,9]
    - Extensive data-editing functionality
    - FEM-based image formation (**Fig. 4**)
  - Various display options, including Automated Anatomical Labeling (AAL) method employed in SPM [10]
  - GLM methods used in support of individual (level 1) and group (level 2) analysis for detection of neuroactivation
  - Atlas-based mapping environment in support of human and macaque studies (**Fig. 5**)
    - Serves as basis for rapid 3D image reconstruction

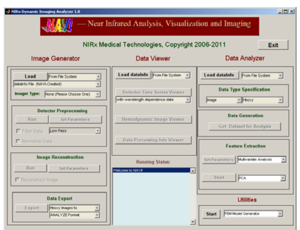

Fig. 3. Screenshot of the NAVI home GUI, used to access menus for data processing and viewing.

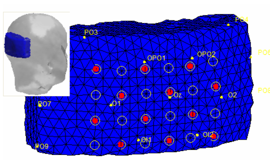

Fig. 4. Graphic of the developed human atlas. Optode sensor array placement displayed on a selected atlas segment is shown, after user-directed or automated specification of optode positions. Open circles represent detector fibers only; filled circles are co-located source and detector. Yellow dots show standard EEG locations.

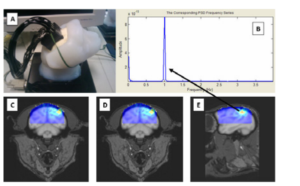

Fig. 5. Example of a testbed imaging study, using a macaque head-shaped dynamic phantom. A: photograph of the phantom with fibers attached. C-E: horizontal, coronal and sagittal views of the reconstructed image, highlighting the location of the ECC. D: after computing the power spectral density of the image time series, the 1 Hz sinusoidal driving function was recovered with negligible distortion.

- Dynamic Causal Modeling / DCM
  - Mathematical strategy for analyzing functional neuroimaging data in order infer effective connectivity [4,5]
  - Chosen over approaches that are exclusively data-driven, because model selection can be reliably guided from prior knowledge [11]
- Experimental study of DCM model selection accuracy, based on analysis of fNIRS time series imaging data
  - Bilinear mathematical model of temporally evolving neuronal activity [5]:

$$\frac{d\mathbf{x}}{dt} = \left[\mathbf{A} + \sum_j u_j \mathbf{B}^{(j)}\right]\mathbf{x} + \mathbf{C}\,\mathbf{u}. \qquad (1)$$

  - $\mathbf{x}$ = time-varying neural activity in a user-specified number of cortical regions

Methods (cont.)

- **A**, **B** and **C** matrices in Eq. (1) specify the effective connectivity, i.e., the effects that activity in one region has on others, and the effects of exogenous inputs **u** on neural activity. (**Fig. 6**)
- For each cortical region, the hemodynamic response to a given value x of neural activity is estimated by means of a neurovascular coupling model [4,9]:

$$\begin{aligned} ds/dt &= x - \kappa s - \gamma(f-1),\\ df/dt &= s, \qquad dv/dt = \left(f - v^{1/\alpha}\right)/\tau, \qquad\qquad (2)\\ dq/dt &= \left\{\left[1-(1-E_0)^{1/f}\right]f/E_0 - (q/v)v^{1/\alpha}\right\}/\tau. \end{aligned}$$

  - s = vasodilatory signal, f = blood flow, q = deoxyhemoglobin content, v = blood volume; κ = vasodilatory signal decay rate, γ = autoregulatory feedback rate constant, τ = mean capillary transit time, α = vessel stiffness exponent, E_0 = capillary resting net oxygen extraction.
- The values of **u** are time-dependent; given the particular **u** in **Fig. 7** and the connectivity pattern depicted in the upper left of **Fig. 6**, solving the coupled differential equations in Eqs. (1) and (2) yields the **v** time series potted in **Fig. 8**.
  - As indicated in **Fig. 8**, the computed **v** time series are used as time-varying voltage signals that drive the ECCs in the dynamic phantom.
  - Higher voltage → darker ECC → lower intensity of light detected in an fNIRS measurement. This mimics the effect of an increase in cerebral blood volume.

Results

- Five sets of fNIRS measurements were carried out, using ECC driving functions computed for each of the models in **Fig. 6**.
- Analyzing the data with NAVI-SPM, using GLM methods from Level-1 SPM, yields statistical parametric maps, such as those shown in **Fig. 9**.
- A spatial mean time series result was generated for each of the driving functions (e.g., **Fig. 8**); subsequently, these served as the input for DCM inverse-problem computations.
  - For each set of experiment-derived data, all five models in **Fig. 6** were evaluated as effective connectivity hypotheses.
  - Based on comparisons of the computed Bayesian evidence (Ref. 5) for each hypothesis, the correct connectivity hypothesis was selected in two of the five cases:

H \ T	1	2	3	4	5
1	91	91	99	93	100
2	100	100	92	95	82
3	81	87	100	92	75
4	51	51	74	87	69
5	71	74	87	100	82

T = Correct (true) connectivity model,
H = DCM connectivity hypothesis

  - In each column, the tabulated numbers are the Bayesian evidence for each hypothesis, as a percentage of the maximal evidence value.
  - Results for the other three cases are affected by unexpected confounding factors: a tendency for DCM to overfit the data noise in some (Model 2), but not all, cases; insufficient degrees of freedom to obtain a good fit to the data in the case of the simplest model (Model 4); absence of a unique solution in the case of the most complex model (Model 5).

Conclusion

- For functional imaging-based DCM, just as for other inverse problems, it is necessary to ensure that the problem is well-posed/conditioned. Accordingly, an important consideration is to appropriately constrain the problem. The availability of an experimental testbed, such as the one described here, facilitates the development and testing of regularization schemes for fNIRS-based DCM.

References

1. Koch, S.P., Habermehl, C., Mehnert, J., Schmitz, C.H., Holtze, S., Villringer, A., Steinbrink, J., Obrig, H. (2010), 'High-resolution optical functional mapping of the human somatosensory cortex', Frontiers in Neuroenergetics, vol. 2, Article 12.
2. Schmitz, C.H., Koch, S.P. (2009), 'Ultracompact, EEG-compatible NIRS system', Poster C 05 at the Berlin Brain Computer Interface Workshop.
3. Gong, G., He, Y., Concha, L., Lebel, C., Gross, D.W., Evans, A.C. Beaulieu, C. (2009), 'Mapping anatomical connectivity patterns of human cerebral cortex using in vivo diffusion tensor imaging tractography', Cerebral Cortex, vol. 19, pp. 524-536.
4. Friston, K.J., Harrison, L., Penny, W. (2003), 'Dynamic causal modelling', NeuroImage, vol. 19, pp. 1273-1302.
5. Penny, W.B., Stephan, K.E., Mechelli, A., Friston, K.J. (2004), 'Comparing dynamic causal models', NeuroImage, vol. 22, pp. 1157-1172.
6. http://www.nirx.net/uploads/Brochures/NIRx_NIRScout.pdf.
7. http://www.brainproducts.com/productdetails.php?id=28&tab=1.
8. Pei, Y., Xu, Y., Barbour, R.L. (2007), 'NAVI-SciPort solution: A problem solving environment (PSE) for NIRS data analysis', Poster No. 221 M-AM at Human Brain Mapping (Chicago, IL, June 10-14, 2007). Available: http://otg.downstate.edu/Publication/PeiHBM07.pdf.
9. NIRx fNIRS Analysis Environment User's guide. Available: http://otg.downstate.edu/Publication/NIRxPackage_02.pdf.
10. Tzourio-Mazoyer, N., Landeau, B., Papathanassiou, D., Crivello, F., Etard, O., Delcroix, N., Mazoyer, B., Joliot, M. (2010), 'Automated anatomical labeling of activations in SPM using a macroscopic anatomical parcellation on the MNI MRI single-subject brain', NeuroImage, vol. 15, pp. 273-289.
11. Friston, K. (2009), 'Causal modeling and brain connectivity in functional magnetic resonance imaging', PLoS Biology, vol. 7, pp. 0220-0225.